Numerical modeling of surface wave development under the action of wind

DMITRY CHALIKOV

Shirshov Institute of Oceanology, Saint Petersburg 199053, Russia

Russian State Hydrometeorological University, SaintPetersburg195196

University of Melbourne, Victoria 3010, Australia

Abstract

The numerical modeling of two-dimensional surface wave development under the action of wind is performed. The model is based on three-dimensional equations of potential motion with free surface written in a surface-following non-orthogonal curvilinear coordinate system where depth is counted from moving surface. Three-dimensional Poisson equation for velocity potential is solved iteratively. Fourier transform method, the second-order accuracy approximation of vertical derivatives on a stretched vertical grid and the fourth-order Runge-Kutta time stepping are used. Both the input energy to waves and dissipation of wave energy are calculated on the basis of the earlier developed and validated algorithms. A one-processor version of the model for PC allows us to simulate an evolution of wave field with thousands of degrees of freedom over thousands of wave periods. A long-time evolution of two-dimensional wave structure is illustrated by the spectra of wave surface and input and output of energy.

1. Introduction

Phase resolving modeling of sea waves is the mathematical modeling of surface waves including explicit simulations of surface elevation and velocity field evolution. Compared with the *spectral wave modeling*, the phase resolving modeling is more general since it reproduces a real visible physical process and is based on the well-formulated full equations. The phase resolving models usually operate with a large number of freedom degrees. In general, this method is more complicated and requires more computational resources. The simplest way of such modeling is the calculation of a wave field evolution based on the linear equations. Such approach allows reproducing the main effects of the linear wave transformation due to superposition of wave modes, reflections, refractions etc. This approach is useful for many technical applications while it cannot reproduce a nonlinear nature of waves and the transformation of wave field due to nonlinearity. Another example of a relatively simple object is a case of the shallow-water waves. The nonlinearity can be taken into account in the more sophisticated models derived from the fundamental fluid mechanics equations with some simplifications. The most popular approach is based on nonlinear Schrödinger equation of different orders (see Dysthe, 1979) obtained by expansion of the *surface wave* displacement. This approach is also used for solving the problem of *freak waves*. The main advantage of a simplified approach is that it allows reducing a three-dimensional (3-D) problem to a two-dimensional one (or 2-D problem to 1-D problem). However, it is not always clear which of the non-realistic effects are eliminated or included in the model after simplifications. This is why the most general approach being developed over the past years is based on the initial two-dimensional or three-dimensional equations (still potential). All the tasks based on these

46 equations can be divided into two groups: the periodic and non-periodic problems. An
47 assumption of periodicity considerably simplifies construction of numerical models though such
48 formulation can be applied to the cases when the condition of periodicity is acceptable, for
49 example, when domain is considered as a small part of a large uniform area. For limited domains
50 with no periodicity the problem becomes more complicated since the Fourier presentation cannot
51 be used directly.

52 From the point of view of physics, the problem of phase resolving modeling can be
53 divided into two groups: the adiabatic and non-adiabatic modeling. A simple adiabatic model
54 assumes that the process develops with no input or output of energy. Being not completely free
55 of limitations, such formulation allows investigating the wave motion on the basis of true initial
56 equations. Including the effects of input energy and its dissipation is always connected with the
57 assumptions that generally contradict an assumption of potentiality, i.e., new terms added to the
58 equations should be referred to as pure phenomenological. This is why treatment of a non-
59 adiabatic approach is often based on quite different constructions.

60 All the phase resolving models use the methods of computational mathematics and inherit
61 all their advantages and disadvantages, i.e., on one side, the possibility of a detailed description
62 of the processes, on the other side, a bunch of the specific problems connected with the
63 computational stability, space and time resolution. Mathematical modeling produces tremendous
64 volumes of information the processing of which can be more complicated than the modeling
65 itself.

66 The phase resolving wave modeling takes a lot of computer time since it normally uses a
67 surface-following coordinate system, which considerably complicates the equations. The most
68 time-consuming part of the model is an elliptic equation for velocity potential usually solved
69 with iterations. Luckily, for a two-dimensional problem this trouble is completely eliminated by
70 use of the conformal coordinates reducing the problem to a one dimensional system of equations
71 which can be solved with high accuracy (Chalikov and Sheinin, 1998). For a three-dimensional
72 problem, the reduction to a two-dimensional form is evidently impossible; hence, the solution of
73 a 3D elliptical equation for velocity potential becomes an essential part of the entire problem.
74 This equation is quite similar to the equation for pressure in a non-potential problem. It follows
75 that the 3-D Euler equations, being more complicated, still can be solved over acceptable
76 computer time.

77 There is a large volume of papers devoted to the numerical methods developed for
78 investigation of wave processes over the past decades. It includes a Finite Difference Method
79 (Engsig-Karup et al., 2009, 2012), , a Finite Volume Method (Causon et al., 2010), a Finite
80 Element Method (Ma and Yan, 2010; Greaves, 2010), a Boundary (Integral) Element Method
81 (Grue and Fructus, 2010), Spectral Methods (Ducroset et al., 2007, 2012, 2016;
82 Touboul and Kharif, 2010; Bonnefoy et al., 2010). These include a Smoothed Particle
83 Hydrodynamics method (Dalrymple et al., 2010), a Large Eddy Simulation Method (LES) (Issa
84 et al., 2010; Lubin and Caltagirone J.-P. (2010), a Moving Particle Semi-implicit method (Kim et
85 al., 2014), a Constrained Interpolation Profile method (Zhao, 2016), a Method of Fundamental
86 Solutions (Young et al., 2010) and a Meshless Local Petrov–Galerkin method (Ma, 2010). Fully
87 nonlinear model should be applied to many problems.. Most of the models were designed for
88 engineering applications such as overturning waves, broken waves, waves generated by
89 landslides, freak waves, solitary waves, tsunamis, violent sloshing waves, interaction of extreme
90 waves with beaches, interaction of steep waves with the fixed structures or with different floating

structures. The references given above make less than one percent of the publications on those topics

Two-dimensional approach (like conformal method) considers a strongly idealized wave field, since even monochromatic waves in the presence of lateral disturbances quickly obtain a two-dimensional structure. The difficulty arising is not a direct result of increase of dimension. The fundamental complication is that the problem cannot be reduced to a two-dimensional problem, and even for the case of a double-periodic wave field the problem of solution of Laplace-like equation for velocity potential arises. The majority of the models designed for investigation of three-dimensional wave dynamics are based on simplified equations such as the second order perturbation methods in which higher order terms are ignored. Overall, it is unclear which effects are missing in such simplified models.

The most sophisticated method is based on full three dimensional equations and surface integral formulations (Beale, 2001; Xue et al., 2001; Grilli et al., 2001; Clamond and Grue, 2001; Clamond et al, 2005, 2006; Fructus et al., 2005; Guyenne et al., 2006; Fochesato et al., 2006). Fully nonlinear, three-dimensional water waves, which extends an approach was suggested by Craig and Sulem (1993) originally given in the two-dimensional setting. The model is based upon Hamiltonian formulation (Zakharov, 1968) which allows reducing a problem of surface variables computation by introducing Dirichlet–Neumann operator which is expressed in terms of its Taylor series expansion in homogeneous powers of surface elevation. Each term in this Taylor series can be obtained from the recursion formula and efficiently computed using fast Fourier transform.

The main advantage of the boundary integral equation methods (BIEM) is that they are accurate and can describe highly nonlinear waves. A method of solution of Laplace equation is based on use of Green's function, which allows us to reduce a 3-D water-wave problem to a 2-D boundary integral problem. The surface integral method is well suited for simulation of the wave effects connected with very large steepness, specifically, for investigation of a freak wave generation. These methods can be applied both to periodic and non-periodic flows. The methods do not impose any limitations on wave steepness, so they can be used for simulation of the waves that even approach breaking (Grilli et al., 2001) when the surface obtains a non-single value shape. The method allows us to take into account bottom topography (Grue and Fructus, 2010) and investigate an interaction of waves with the fixed structures or with the freely-responding floating structures (Liu et al., 2016, Gou et al., 2010).

However, the BIEM method seems to be quite complicated and time-consuming being applied to a long-term evolution of a multi-mode wave field in large domains. The simulation of relatively simple wave fields illustrates an application of the method, and it is unlikely that the method can be applied to the simulation of a long-term evolution of a large-scale multi-mode wave field with a broad spectrum. Implementation of a multi-pole technique for a general problem of the sea wave simulation (Fochesato et al., 2006) can solve the problem but obviously leads to the considerable algorithmic difficulties.

Currently, the most popular in oceanography approach is a HOS (High Order Scheme) model developed by Dommermuth and Yue (1987); West et al. (1987). The HOS is based on a paper by Zakharov (1968), where a convenient form of the dynamic and kinematic surface conditions was suggested. Equations used by Zakharov were not intended for modeling, but rather for investigation of stability of finite amplitude waves. In fact, a system of coordinates where depth is counted from the surface, was used, but the Laplace equation for velocity

136   potential was taken in its traditional form. However, the Zakharov's followers have accepted this

137   idea literally. They used two coordinate systems: a curvilinear surface-fitting system for surface

138   conditions and the Cartesian system for calculation of a surface vertical velocity. The analytic

139   solution for velocity potential in the Cartesian coordinate system is known. It is based on the

140   Fourier coefficients on a fixed level, while the true variables are the Fourier coefficients for the

141   potential on a free surface. Here a problem of transition from one coordinate system to another

142   arises. This problem is solved by expansion of the surface potential into the Taylor series in the

143   vicinity of the surface. An accuracy of this method depends on that of representation of an

144   exponential function with a finite number of the Taylor series. For the small-amplitude waves

145   and for a narrow wave spectrum, such accuracy is evidently satisfactory. However, for the case

146   of a broad wave spectrum that contains many wave modes, the order of the Taylor series should

147   be high. The problem is now that the waves with high wave numbers are superposed over the

148   surface of larger waves. Since the amplitudes of a surface potential attenuate exponentially, an

149   amplitude of a small wave at a positive elevation increases, and on the contrary, it can approach

150   zero at negative elevations. It is clear that such setting of HOS model cannot reproduce high-

151   frequency waves, which actually reduces the nonlinearity of the model. This is why such model

152   can be integrated for long periods using no high frequency smoothing. Besides, an accuracy of

153   calculation of vertical velocity on the surface depends on full elevation at each point. Hence, the

154   accuracy is not uniform along a wave profile. A substantial increase of the Taylor expansion

155   order can definitely result in the numerical instability due to occasional amplification of modes

156   with high wave numbers. The authors of a surface integral method shared a similar point of view

157   (Clamond et al., 2005). We should note, however, that comparison of HOS method based on the

158   West et al., (1987) approach using a method of the surface integral for an idealized wave field

159   (Clamond et al., 2006) shows quite acceptable results. It was shown in the previous paper that a

160   method suggested by Dommermuth et al., (1987) demonstrates poorer divergence of the

161   expansion for vertical velocity than for method by West et al., (1987). The HOS model has been

162   widely used (for example, Tanaka, 2001; Toffoli et al., 2010; Touboul and Kharif, 2010) and it

163   has shown its ability to efficiently simulate the wave evolution (propagation, nonlinear wave–

164   wave interactions, etc.) in a large-scale domain (Ducrozet et al., 2007, 2012). It is obvious that

165   the HOS model can be used for many practical purposes. Recently, Ecole Centrale Nantes,

166   LHEEA Laboratory (CNRC) announced that the non-linear wave models based on High-Order

167   Spectral (HOS) are published as an open source (https://github.com/LHEEA/HOS-ocean/wiki).

168   Opposite to the HOS method based on the analytical solution of Laplace equation in the

169   Cartesian coordinates, a group of models is based on direct solution of the equation for velocity

170   potential in the curvilinear coordinates (Engsig-Karup et al, 2009, 2012; Chalikov et al., 2014).

171   The main advantage of the surface-following coordinate system is that a variable surface is

172   mapped onto the fixed plane. Since wave motion is very conservative, the high accuracy

173   numerical schemes should be used for a good description of nonlinearity and spectrum

174   transformation. This most universal approach is being developed at the Technical University of

175   Denmark (see Engsig-Karup, 2009). Actually, the models *ModelWave3D* developed at TUD are

176   targeted at solution of a variety of problems including such problems as modeling of wave

177   interaction with submerged objects as well as the simulation of wave regime in the basins with

178   real shape and topography.

179   The model is based on the equations of potential flow with a free surface. An effect of

180   variable bathymetry is taken into account by using a so-called σ-coordinate,

181 (straightening out the bottom and surface). At vertical surfaces a normal derivative of the
182 velocity potential is equal to zero. A flexible-order approximation for spatial derivatives is used.
183 The most time-consuming part of this mode is a 3-D equation for the velocity potential. The
184 strategy of the model development is directed at exploiting architectural features of modern
185 GPUs for the mixed precision computations. This approach is tested using a recently developed
186 generic library for fast prototyping of PDE (Partial Differential Equations) solvers. The new
187 wave tool is applicable for solving and analyzing of a variety of large-scale wave problems in the
188 coastal and offshore engineering. A description of the project and references can be found at site
189 (http://www2.compute.dtu.dk/~apek/OceanWave3D/).

190 Comparison of *ModelWave3D* with HOS model was presented by Ducrozet et al., (2012).
191 It was shown that both model demonstrate high accuracy, but HOS model shows better
192 performance. Note, that comparison of speed of models in this case is not indicative since
193 *ModelWave3D* was designed for investigation of complicated processes, taking into account the
194 real shape of basin, variable depth and even presence of engineering constructions. All these
195 features obviously are not included in HOS model.

196 Development of waves under the action of wind is a process that is difficult to simulate
197 since surface waves are very conservative and change their energy for hundreds and thousands of
198 periods. This is why the most popular method is spectral modeling. Waves as physical objects in
199 this approach are actually absent, since evolution of spectral distribution of wave energy is
200 simulated. The description of input and dissipation in this approach is not connected directly
201 with the formulation of the problem, but it is rather adopted from other branches of wave theory
202 where waves are the objects of investigation. However, the spectral approach turned out to be the
203 only method capable of describing the space and time evolution of wave field in the ocean. The
204 phase resolving models (or 'direct' models) designed for reproducing waves themselves cannot
205 compete with spectral models since a typical size of domain in such models does not exceed
206 several kilometers. Such domain includes just several thousands of large waves. Nevertheless,
207 direct wave modeling plays an ever-increasing role in geophysical fluid dynamics, because it
208 gives the possibility to investigate the processes which cannot be reproduced with spectral
209 models. One of such problems is that of extreme wave generation. (Chalikov, 2009; Chalikov,
210 and Babanin, 2016a). Direct modeling is also a perfect instrument for development of
211 parameterization of physical processes for spectral wave models. Besides, such models can be
212 used for direct simulation of wave regimes of small water basins, for example, port harbors.
213 Other approaches of direct modeling are discussed in (Chalikov et al., 2014; Chalikov, 2016)

214 Until recently, direct modeling was used for reproduction of quasi-stationary wave
215 regime when wave spectrum essentially did not change. An unique example of direct numerical
216 modeling of surface wave evolution is given in Chalikov and Babanin (2014)where development
217 of wave field was calculated with use of a two-dimensional model based on full potential
218 equations written in the conformal coordinates. The model included algorithms for
219 parameterization of input and dissipation of energy (a description of similar algorithms is given
220 below). The model successfully reproduced an evolution of wave spectrum under the action of
221 wind. However, strictly one-dimensional (unidirected) waves are not realistic; hence, the full
222 problem of wave evolution should be formulated on the basis of three-dimensional equations. An
223 example of such modeling is given in the current paper.

224

225 **2. Equations**

226

227   Let us introduce a *non-stationary surface-following non-orthogonal* coordinate system:

228    $\xi = x, \quad \vartheta = y, \quad \zeta = z - \eta(\xi, \vartheta, \tau), \quad \tau = t$,   (1)

229   where $\eta(x, y, t) = \eta(\xi, \vartheta, \tau)$ is a moving periodic wave surface given by the Fourier series

230    $$\eta(\xi, \vartheta, \tau) = \sum_{-M_x < k < M_x} \sum_{-M_y < l < M_y} h_{k,l}(\tau) \Theta_{k,l},$$ (2)

231   where k and l are components of wave number vector k, $h_{k,l}(\tau)$ are Fourier amplitudes for

232   elevations $\eta(\xi, \vartheta, \tau)$, M_x and M_y are the numbers of modes in directions ξ and ϑ, respectively,

233   while $\Theta_{k,l}$ are Fourier expansion basis functions, represented as matrix:

234
$$\Theta_{kl} = \begin{cases} \cos(k\xi + l\vartheta) & -M_x \le k \le M_x, -M_y < l < 0 \\ \cos(k\xi) & -M_x \le k \le 0, l = 0 \\ \sin(k\xi) & 0 \le k \le M_y, l = 0 \\ \sin(k\xi + l\vartheta) & -M_x \le k \le M_x, 0 < l \le M_y \end{cases}$$ (3)

235   The 3-D equations of potential waves in the system of coordinates (1) at $\zeta \le 0$ take the

236   following form:

237    $\eta_\tau = -\eta_\xi \varphi_\xi - \eta_\vartheta \varphi_\vartheta + \left(1 + \eta_\xi^2 + \eta_\vartheta^2\right) \Phi_\varsigma$,   (4)

238    $\varphi_\tau = -\dfrac{1}{2}\left(\varphi_\xi^2 + \varphi_\vartheta^2 - \left(1 + \eta_\xi^2 + \eta_\vartheta^2\right)\Phi_\zeta^2\right) - \eta - p$,   (5)

239    $\Phi_{\xi\xi} + \Phi_{\vartheta\vartheta} + \Phi_{\zeta\zeta} = \Upsilon(\Phi)$,   (6)

240   where Υ is the operator:

241    $\Upsilon() = 2\eta_\xi ()_{\xi\zeta} + 2\eta_\vartheta ()_{\vartheta\zeta} + \left(\eta_{\xi\xi} + \eta_{\vartheta\vartheta}\right)()_\zeta - \left(\eta_\xi^2 + \eta_\vartheta^2\right)()_{\zeta\zeta}$,   (7)

242   capital fonts Φ are used for domain $\zeta < 0$ while the lower case φ refers to $\zeta = 0$. Term p in (5)

243   described the pressure on surface $\zeta = 0$.

244   It is suggested in (Chalikov et al., 2014) that it is convenient to represent velocity

245   potential φ as a sum of two components, i.e., an analytical ('linear') component

246    $\bar{\Phi}, \left(\bar{\varphi} = \bar{\Phi}(\xi, \vartheta, 0)\right)$ and an arbitrary ('non-linear') component $\tilde{\mathsf{F}}, \left(\tilde{\jmath} = \tilde{\mathsf{F}}(x, \jmath, 0)\right)$:

247    $\jmath = \bar{\jmath} + \tilde{\jmath}, \quad \mathsf{F} = \bar{\mathsf{F}} + \tilde{\mathsf{F}}$.   (8)

248   The analytical component $\bar{\Phi}$ satisfies Laplace equation:

249    $\bar{\Phi}_{\xi\xi} + \bar{\Phi}_{\vartheta\vartheta} + \bar{\Phi}_{\zeta\zeta} = 0$,   (9)

250   with known solution:

251    $$\bar{\Phi}(\xi, \vartheta, \zeta, \tau) = \sum_{k,l} \bar{\varphi}_{k,l}(\tau) \exp\left(|k|\zeta\right) \Theta_{k,l},$$ (10)

252   (where $|k| = \left(k^2 + l^2\right)^{1/2}$, $\bar{\varphi}_{k,l}$ are Fourier coefficients of surface analytical potential $\bar{\varphi}$ at $\zeta = 0$).

253   The solution satisfies boundary conditions:

254    $\varsigma = 0: \quad \bar{\Phi} = \bar{\varphi}$
       $\varsigma \to -\infty: \quad \tilde{\Phi}_\zeta \to 0$ (11)

255   The nonlinear component satisfies an equation:

256    $\tilde{\Phi}_{\xi\xi} + \tilde{\Phi}_{\vartheta\vartheta} + \tilde{\Phi}_{\zeta\zeta} = \Upsilon(\tilde{\Phi}) + \Upsilon(\bar{\Phi})$,   (12)

257   Eq. (12) is solved with the boundary conditions:

258
$$\varsigma = 0: \quad \tilde{\Phi} = 0$$
$$\varsigma \to -\infty: \quad \tilde{\Phi}_\varsigma \to 0 \tag{13}$$

259   The derivatives of linear component $\bar{\Phi}$ in (7) are calculated analytically. The scheme
260 combines 2-D Fourier transform method in the 'horizontal surfaces' and a second-order finite-
261 difference approximation on a stretched staggered grid defined by relation $\Delta\zeta_{j+1} = \chi\Delta\zeta_j$ ($\Delta\zeta$ is
262 a vertical step, while $j=1$ at the surface). The stretched grid provides increase of accuracy of
263 approximation for the exponentially decaying modes. The values of stretching coefficient χ lie
264 within the interval 1.01-1.20. A finite-difference second-order approximation of vertical
265 operators in Eq. (12) on a non-uniform vertical grid is quite straightforward. Equation (12) is
266 solved as Poisson equations with iterations over the right-hand side. A each time step the
267 iterations start with right-side calculated at previous time step. The initial elevation was
268 generated as superposition of linear waves corresponding to JONSWAP spectrum (Hasselmann
269 et al., 19734) with random phases. The initial Fourier amplitudes for surface potential were
270 calculated by formulas of linear wave theory. A detailed description of the scheme and its
271 validation is given in Chalikov et al., (2014) and Chalikov (2016).

272   Equations (4) – (6) are written in a non-dimensional form by using the following scales:
273 length L where $2\pi L$ is (dimensional) period in the horizontal direction; time $L^{1/2}g^{-1/2}$ and velocity
274 potential $L^{3/2}g^{1/2}$ (g is acceleration of gravity). The pressure is normalized by water density, so
275 that the pressure scale is Lg. Equations (4) – (6) are self-similar to the transformation with
276 respect to L. The dimensional size of domain $2\pi L$, so scaled size is 2π. All the results
277 presented in this paper are nondimensional. Note that the number of Fourier modes can be
278 different in x and y directions. In this case is assumed that two length scales L_x and L_y are used.
279 The nondimensional length of domain in y-direction remains equal 2π and factor $r = L_x / L_y$ is
280 introduced in definition of differentiation in Fourier space.

281
282   **3. Energy input and dissipation**
283

284   Input energy to waves describes a pressure term p in a dynamic boundary condition (5).
285 The tangent stress on the surface cannot be taken into account in potential formulation.
286 Dissipation cannot be also described with use of potential equations, but for realistic description
287 of wave dynamics, dissipation of wave energy should be taken into account, i.e., we should
288 include in equations (4) and (5) additional terms which, strictly speaking, contradict the
289 assumption of potentiality.

290   **3.1 Energy input from wind**

291   According to the linear theory(Miles, 1957), the Fourier components of surface pressure
292 p are connected with those of surface elevation through the following expression:

293
$$p_{k,l} + \mathrm{i}p_{-k,-l} = \frac{\rho_a}{\rho_w}\left(\beta_{k,l} + \mathrm{i}\beta_{-k,-l}\right)\left(h_{k,l} + \mathrm{i}h_{-k,-l}\right), \tag{14}$$

294 where $h_{k,l}, h_{-k,-l}, \beta_{k,l}, \beta_{-k,-l}$, are real and imaginary parts of elevation η and the so-called β-
295 function (i.e., Fourier coefficients at COS and SIN, respectively); ρ_a / ρ_w is a ratio of air and

water densities. Eq. (14) is a standard presentation of pressure above multi-mode surface. It means that every wave mode with amplitude $\left(h_{k,l}^2 + h_{-k,-l}^2\right)^{1/2}$ initiates the pressure mode with amplitude $\left(p_{k,l}^2 + p_{-k,-l}^2\right)^{1/2}$ shifted by phase of wave mode by angle $\alpha = \mathrm{atan}\, \dfrac{\beta_{-k,-l}}{\beta_{k,l}}$. Both coefficients in (14) are function of ratio of wind velocity at half of mode length height $\lambda_{k,l}/2$ to virtual phase velocity. Hence, for derivation of shape of beta-function it is necessary to simultaneously measure wave surface elevation and non-static pressure on the surface. Experimental measurement of surface pressure is a very difficult problem since the measurements should be done very close to a moving surface, preferably, with a surface-following sensor. Such measurements are done quite seldom, especially, in the field. The measurements were carried out for the first time by a team of authors both in laboratory and field (Snyder et al, 1981; Hsiao and Shemdin, 1983; Hasselmann and Bösenberg, 1991; Donelan et al., 2005, 2006). The data obtained in this way allowed constructing an imaginary part of beta-function used in some versions of wave forecasting models (Rogers et al., 2012). Such measurements and their processing are quite complicated since wave-produced pressure fluctuations are masked by turbulent pressure fluctuations. The second way of beta-function evaluation is based on the results of numerical investigations of statistical structure of the boundary layer above waves with use of Reynolds equations and an appropriate closure scheme. In general, this method works so well that many problems in the technical fluid mechanics are often solved using numerical models, not experimentally (Gent and Taylor, 1976; Riley et al. 1982; Al-Zanaidi and Hui, 1984).. This method was being developed beginning from (Chalikov, 1978, 1986), followed by (Chalikov and Makin, 1991; Chalikov and Belevich, 1992; Chalikov, 1995). The results were implemented in WAVEWATCH model, i.e., a third-generation wave forecast model (Tolman and Chalikov, 1996) and thoroughly validated against the experimental data in the course of developing WAVEWATCH-III (Tolman et al., 2014). This method was later improved on the basis of more advanced coupled modeling of waves and boundary layer (Chalikov and Rainchk, 2010), while the beta-function used in WAVEWATCH-III was corrected and extended up to high frequencies. Direct calculation of energy input to waves requires both real and imaginary parts of the beta-function. The total energy input to waves depends on imaginary part of β-function, while the moments of higher order depend both on imaginary and real parts of β. This is why full approximation constructed in (Chalikov and Rainchik, 2010) was used in the current work. Note that in the range of relatively low frequencies the nw method is very close to the scheme implemented in WAVEWATCH-III.

It is a traditional suggestion that both coefficients are the functions of virtual nondimensional frequency $\Omega = \omega_{k,l} U \cos\psi = U / c_{k,l} \cos\psi$ (where $\omega_{k,l}$ and U are the nondimensional radian frequency and wind speed, respectively; $c_{k,l}$ is a phase speed of the kth mode; ψ is an angle between wind and wave mode directions). Most of the schemes for calculations of β-function consider a relatively narrow interval of nondimensional frequencies Ω. In the current work, the range of frequencies covers an interval $\left(0 < \Omega < 10\right)$, and occasionally the values of $\Omega > 10$ can appear. This is another reason why the function derived in (Chalikov and Rainchik, 2010) through coupled simulations of waves and boundary layer, is used here. Wave model is based on potential equations for a flow with free surface, extended

337 with an algorithm for breaking dissipation (see below description of the breaking dissipation
338 parameterization). Wave boundary layer (WBL) model is based on Reynolds equations closed
339 with $K - \varepsilon$ scheme; solutions for air and water are matched through the interface. The β-
340 function was used for evaluation of accuracy of the surface pressure p calculations. A shape of
341 β-function connecting surface elevations and surface pressure, is studied up to high
342 nondimensional wave frequencies both in positive and negative (i.e., for wind opposite to waves)
343 domains. The data on β-function exhibit wide scatter, but since the volume of data was quite
344 large (47 long-term numerical runs allowed us to generate about 1,400,000 values of β), the
345 shape of β-function was defined with satisfactory accuracy up to very high nondimensional
346 frequencies $(-50 < \Omega < 50)$. As a result, the data on β-function in such a broad range, allow us
347 to calculate wave drag up to very high frequencies and to explicitly divide the fluxes of energy
348 and momentum transferred by the pressure and molecular viscosity. This method is free of
349 arbitrary assumptions on the drag coefficient C_d; and, on the other hand, such calculations allow
350 investigating the nature of wave drag (see Ting et al., 2012).
351   The most reliable data on β-function are concentrated in interval $-10 < \Omega < 10$ (negative
352 values of Ω correspond wave modes running against wind). real and imaginary parts of beta
353 function are shown in Fig. (1). It is an corrected version of approximation given in Chalikov and
354 Rainchik (2010), where data at negative Ω were interpreted erroneously. In current calculations
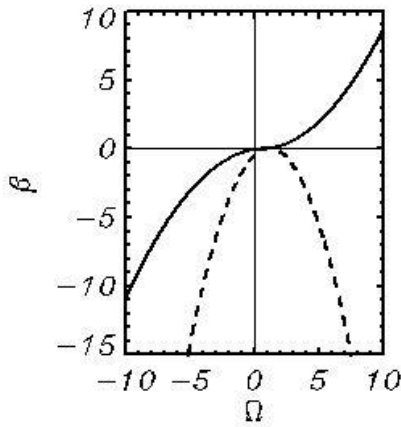355 the modes running against wind are absent.
356

Figure 1. Real (dashed curve) and imaginary (solid curve) parts of β-function.

368

369 Function β can be approximated by formulas:

370

371
$$\beta_{k,l} = \begin{cases} \beta_0 + a_0 (\Omega - \Omega_0) + a_1 (\Omega - \Omega_0)^2 & \Omega_0 < \Omega \\ \beta_0 + a_0 (\Omega - \Omega_0) - a_1 (\Omega - \Omega_0)^2 & \Omega < \Omega_0 \end{cases}, \tag{15}$$

372
$$\beta_{-k,-l} = \begin{cases} \beta_1 + a_3 (\Omega - \Omega_2) & \Omega < \Omega_2 \\ a_2 (\Omega - \Omega_1)^2 & \Omega_2 < \Omega < \Omega_3 \\ \beta_1 - a_3 (\Omega - \Omega_3) & \Omega_3 < \Omega \end{cases}, \tag{16}$$

9

where the coefficients are:

$\Omega_0 = 0.02277, \Omega_1 = 1.20, \Omega_2 = -18.8, \Omega_3 = 21.2, a_0 = 0.02277, a_1 = 0.09476, a_2 = -0.3718,$
$a_3 = 14.80, b_0 = -0.02, b_1 = -148.0.$

It was indicated above that an initial wave field is assigned as superposition of linear modes of which amplitudes are calculated with JONSWAP spectrum with initial peak wave number $k_p^0 = 100$. The initial value $U/c_p^0 = 6$ was chosen, i.e., a ratio of the nondimensional wind speed at height of half of initial peak wave length $\lambda_0/2 = 2\pi/100$ and the phase speed $c_p^0 = \left(k_p^0\right)^{-1/2}$ is equal to 6. Such a high ratio corresponds to initial stages of wave development. Wind velocity $6c_p^0$ remains constant during all time of integration. The values of Ω for other wave numbers are calculated by assuming that wind profile is logarithmic:

$$\Omega_{k,l} = \frac{U}{c_{k,l}} \ln \frac{\lambda_{k,l}}{2z_0} \left(\ln \frac{\lambda_0}{2z_{00}} \right)^{-1} \cos \psi_{k,l}, \qquad (17)$$

where z_{00} is effective nondimensional roughness for the initial wind profile, while z_0 is the actual roughness parameter that depends on the energy in a high-frequency part of spectrum and on the wind profile. We call it 'effective', since very c, lose to the surface the wind profile is not logarithmic (Chalikov, 1995; Tolman and Chalikov, 1996; Chalikov and Rainchik, 2010). The value of this parameter depends on the wind velocity and energy in a high-wave number interval of wave spectrum, as well as on the length scale of the problem. All these effects are possible to include by matching the wave model with a one dimensional WBL model(Ting et al., 2012). Here, a simplified scheme for the roughness parameter is chosen. It is well known that the roughness parameter (as well as a drag coefficient) increases with decrease of the inverse wave age. In our case wind speed is fixed, and dependence for the nondimensional roughness parameter is constructed on the basis of the results obtained in (Chalikov and Rainchik, 2010):

$$z_0 = 15 z_{00} \Omega, \qquad (18)$$

where $z_{00} = 10^{-3}$ is the initial value of the roughness parameter. Eq. (18) approximates dependence of the effective roughness at the stage of wave development. Note that the results are not sensitive to variation of the roughness parameter within reasonable limits.

3.2 High wave number energy dissipation

A nonlinear flux of energy directed to the small wave numbers produces downshifting of spectrum, while an opposite flux forms a shape of spectral tail. The second process can produce accumulation of energy near 'cut' wave number. Both processes become more intensive with increase of energy input. Growth of amplitudes at high wave numbers is followed by the growth of local steepness and numerical instability. This well-known phenomenon in numerical fluid mechanics is eliminated by use of a highly selective filter simulating nonlinear viscosity. To support stability, additional terms are included into the right hand sides of equations (4) and (5):

$$\frac{\partial \eta_{k,l}}{\partial \tau} = E_{k,l} - \mu_{k,l} \eta_{k,l}, \qquad (19)$$

$$\frac{\partial \varphi_{k,1}}{\partial \tau} = F_{k,l} - \mu_{k,l} \varphi_{k,l} \qquad (20)$$

410

411 ($E_{k,l}$ and $F_{k,l}$ are Fourier amplitudes of the right-hand sides of equations (4) and (5) while factor

412 $\mu_{k,l}$ is calculated using a formula:

413
$$\mu_{k,l} = \begin{cases} 0 & |k| < k_d \\ c_m k_0 \left(\dfrac{|k| - k_d}{(k_0 - k_d)} \right)^2 & k_d \le |k| \le k_0 \\ c_m k_0 & |k| > k_0 \end{cases} \qquad (21)$$

414 where k and l are components of wave number $|k|$, while coefficients k_d and k_0 are defined by the

415 expressions:

416
$$k_d = d_m^2 M_x M_y \left(\left(l|k|^{-1} d_m M_x \right)^2 + \left(k|k|^{-1} d_m M_y \right)^2 \right)^{-1/2} \qquad (22)$$

417
$$k_0 = M_x M_y \left(\left(l|k|^{-1} M_x \right)^2 + \left(k|k|^{-1} M_y \right)^2 \right)^{-1/2} \qquad (23)$$

418 where $c_m = 0.1$, $d_m = 0.75$. Expressions (18) - (20) can be interpreted in a straightforward way:

419 the value of $\mu_{k,l}$ is equal to zero inside the ellipse with semi-axes $d_m M_x$ and $d_m M_y$; then it grows

420 linearly with $|k|$ up to the value c_m and is equal to c_m outside the outer ellipse. This method of

421 filtration that we call 'tail dissipation' was developed and validated with a conformal model by

422 Chalikov and Sheinin (1998). The sensitivity of the results to the parameters in (21) - (23) is not

423 high. The aim of the algorithm is support of smoothness and monotonicity of wave spectrum

424 within a high wave number range. Since the algorithm affects the amplitudes of small modes, it

425 actually does not reduce the total energy, though it efficiently prevents development of

426 numerical instability. Note that any long-term calculations cannot be performed without 'tail

427 dissipation' eliminating development of the numerical instability at high wave numbers.

428

429 **3.3 Dissipation due to wave breaking**

430

431 The main process of wave dissipation is wave breaking. This process is taken into

432 account in all spectral wave forecasting models similar to WAVEWATCH (see Tolman and

433 Chalikov, 1996).Since there are no waves in spectral models, no local criteria of wave breaking

434 can be formulated. This is why breaking dissipation is represented in spectral models in a

435 distorted form. A real breaking occurs in relatively narrow areas of physical space; however,

436 spectral image of such breaking is stretched over the entire wave spectrum, while in reality the

437 breaking decreases height and energy of dominant waves. This contradiction occurs because

438 waves in spectral models are assumed as linear ones, while in fact the breaking occurs in

439 physical space with nonlinear sharp wave, usually composed of several modes. However,

440 progress has been gradually made in spectral wave modeling over the past decade. One important

441 outcome is that the wave breaking term in the state-of-art wave models now accounts for the threshold-

442 behavior of dominant wave breaking, that is, waves won't break unless their steepness exceeds a threshold

443 (Alves and Banner, 2003; Babanin et al., 2010).

444 The mechanics of wave breaking at developed wave spectrum differs from that in a wave

445 field represented by few modes, normally considered in many theoretical and laboratory

446 investigations (e.g., Alberello et al., 2018). Since the breaking in laboratory conditions is initiated

11

by special assigning of amplitudes and phases, it cannot be similar to the breaking in natural conditions. To some degree, the wave breaking is similar to development of extreme wave that appears suddenly with no pronounced prehistory (Chalikov and Babanin, 2016a, 2016b). There are no signs of modulational instability in both phenomena, which suggests a process of taking energy from other modes. The evolution leading to breaking or 'freaking' seems just opposite: full energy of main wave remains nearly constant while the columnar energy is focusing around the crest of this wave which becomes sharper and unstable. Probably, even more frequent cases of wave breaking and extreme wave appearance can be explained by local superposition of several modes.

The instability of interface leading to breaking is an important and poorly developed problem of fluid mechanics. In general, this essentially nonlinear process should be investigated for a two-phase flow. Such approach was demonstrated, for example, by Iafrati (2001). However, the progress in solving this highly complicated problem is not too fast.

The problem of breaking parameterization includes two points: (1) establishing of a criterion of breaking onset and (2) developing of an algorithm of breaking parameterization. The problem of breaking is discussed in details in Babanin (2011). Chalikov and Babanin (2012) performed numerical investigation of the processes leading to breaking. It was found that a clear predictor of breaking, formulated in dynamical and geometrical terms, probably does not exist. The most evident criterion of breaking is the breaking itself, i.e., the process when some part of upper portion of sharp wave crest is falling down. This process is usually followed by separation of detached volume of liquid into water and air phases. Unfortunately, there is no possibility to describe this process within the scope of potential theory.

Some investigators suggest using the physical velocity approaching the rate of surface movement in the same direction as a criterion of breaking onset. This is incorrect, since the kinematic boundary condition suggests that these quantities are exactly equal to each other. It is quite clear that the onset of breaking can be characterized by appearance of non-single-value piece of surface. This stage can be investigated with two-dimensional model which due to a high flexibility of the conformal coordinates allows us to reproduce a surface with the inclination in the Cartesian coordinates larger than 90 degrees. (In the conformal coordinates the dependence of elevation on curvilinear coordinate is always single-value). The duration of this stage is extremely short, the calculations being always interrupted by the numerical instability with sharp violation of conservations laws (constant integral invariants, i.e., full energy and volume) and strong distortion of the local structure of flow. Numerous numerical experiments with conformal model showed that after appearance of non-single value, the model never returns to stability. However, introducing of appearance of the non-single-surface as a criterion of breaking instability even in conformal model is impossible, since a behavior of model at a critical point is unpredictable, and the run is most likely to be terminated, no matter what kind of parameterization of breaking is introduced. It means that even in a precise conformal model, stabilization of solution should be initiated prior to breaking.

Consideration of exact criterion for breaking onset for the models using transformation of the coordinate type of (1) is useless, since the numerical instability in such models arises not because of the breaking approaching but because of appearance of large local steepness. Multiple experiments with direct 3-D wave model show that appearance of local steepness $\max\left(\frac{\partial \eta}{\partial x}, \frac{\partial \eta}{\partial y}\right)$ exceeding ≈ 2 (that corresponds to a slope of about 60 degrees) is always

followed by numerical instability but instability can happen far before reaching this value. Decrease of time step does not make any effect. As seen, a surface with such slope is very far from being a vertical 'wall', when real breaking starts. However, an algorithm for breaking parameterization must prevent a numerical instability. The situation is similar to the numerical modeling of turbulence (LES technique), where the local highly selective viscosity is used to prevent appearance of too large local gradients of velocity. The description of breaking in direct wave modeling should satisfy the following conditions. (1) It should prevent the onset of instability at each point of half million of grid points over more than 100 thousand of time steps.(2) It should describe in a more or less realistic way the loss of kinetic and potential energies with preservation of balance between them. (3) It should preserve the volume. It was suggested in (Chalikov, 2005) that an acceptable scheme can be based on the local highly selective diffusion operator with special diffusion coefficient. Several schemes of such type were validated, and finally the following scheme was chosen:

$$\eta_\tau = E_\eta + J^{-1}\left(\frac{\partial}{\partial \xi} B_\xi \frac{\partial \eta}{\partial \xi} + \frac{\partial}{\partial \vartheta} B_\vartheta \frac{\partial \eta}{\partial \vartheta} \right), \tag{24}$$

$$\varphi_\tau = F_\varphi + J^{-1}\left(\frac{\partial}{\partial \xi} B_\xi \frac{\partial \varphi}{\partial \xi} + \frac{\partial}{\partial \vartheta} B_\vartheta \frac{\partial \varphi}{\partial \vartheta} \right), \tag{25}$$

where F_η and F_φ are the right-hand sides of equations (4) and (5) including the terms introduced in terms of Fourier coefficients by (19) − (23), B_ξ and B_ϑ are diffusion coefficients. It was suggested in the first versions of the scheme that diffusion coefficient depends on a local slope, however, such scheme did not prove to be very reliable since it did not prevent all of the events of numerical instability. A scheme based on the calculation of the local curvilinearity $\eta_{\xi\xi}$ and $\eta_{\vartheta\vartheta}$ turned out to be a lot more robust. The calculations of 75 different runs were performed with full 3-D model in (Chalikov et al., 2014) over period of $t = 350$ (70,000 time steps). The total number of values used for the calculations of dependence in Fig. 2 (thick curve) is about 6 billion. The normal probability calculated with the same dispersion is shown by thin curve.
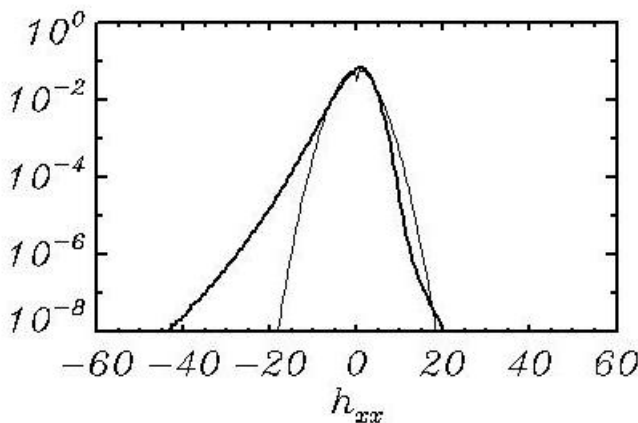
515

Figure 2. Probability of curvilinearity $\eta_{\xi\xi}$. Thick curve calculated with full 3-D model; thin curve is a probability calculated over ensemble of linear modes with the same spectrum.

527

It is seen that the probability of large negative values of curvilinearity is by orders larger than the probability calculated over ensemble of linear modes with spectra generated by nonlinear model.

The curvilinearity turned out to be very sensitive to the shape of surface. This is why it

13

was chosen as a criterion of breaking approach. Coefficients B_ξ and B_ϑ depend nonlinearly on the curvilinearity

$$B_\xi = \begin{cases} \Delta\xi C_B \eta_{\xi\xi}^2 & \eta_{\xi\xi} < \eta_{\xi\xi}^{cr} \\ 0 & \eta_{\xi\xi} \geq \eta_{\xi\xi}^{cr} \end{cases} \tag{26}$$

$$B_\vartheta = \begin{cases} \Delta\vartheta C_B \eta_{\vartheta\vartheta}^2 & \eta_{\vartheta\vartheta} < \eta_{\xi\xi}^{cr} \\ 0 & \eta_{\vartheta\vartheta} \geq \eta_{\xi\xi}^{cr} \end{cases} \tag{27}$$

where $\Delta\xi$ and $\Delta\zeta$ are horizontal steps in x and y direction in grid space, and coefficients are $C_B = 2.0$, $\eta_{\xi\xi}^{cr} = \eta_{\vartheta\vartheta}^{cr} = -50$. Algorithm (24) - (27) does not change the volume and decreases the local potential and kinetic energy. It is assumed that the lost momentum and energy are transferred to current and turbulence (see Chalikov and Belevich, 1992). Besides, the energy also goes to other wave modes. The choice of parameters in (24) - (27) is based on simple considerations: local piece of surface can closely approach the critical curvilinearity but not exceed it. The values of the coefficients are picked with reserve to provide stability of long runs.

We do not think that the suggested breaking parameterization is a final solution of the problem. Other schemes will be tried in the next version of the model. However, the results presented below show that the scheme is reliable and provides a realistic energy dissipation rate.

4. Calculations and results

The elevation and surface velocity potential fields are approximated in the current calculations by $M_x = 256$ and $M_y = 128$ modes in directions x and y. The corresponding grid includes $N_x \times N_y = (1024 \times 512)$ knots. The vertical derivatives are approximated at vertical stretched grid $d\zeta_{j+1} = \chi d\zeta_j$, $(j = 1, 2, 3..., L_w)$ where $\nu = 1.2$ and $L_w = 10$. The small number of levels used for solution of the equation for nonlinear component of the velocity potential is possible because just a surface vertical derivative for the velocity potential $\partial\Phi / \partial\zeta\,(\zeta = 0)$ is required. The velocity potential mainly consists of an analytical component $\bar{\varphi}$, while a nonlinear component provides but small correction. To reach an accuracy of solution $\varepsilon = 10^{-6}$ for equation (11), no more than two iterations were usually sufficient.

The parameters chosen were used for solution of the problem of wave field evolution over acceptable time (of the order of 10 days). The initial conditions were assigned on the basis of empirical spectrum JONSWAP (Hasselmann et al., 1973) with a maximum placed at wave number $k_p = 100$ with angle spreading $(\cosh\psi)^{256}$. Details of initial conditions are of no importance because an initial energy level is quite low.

The total energy of wave motion $E = E_p + E_k$ (E_p - is potential energy, while E_k is kinetic energy) is calculated with the following formulas:

$$E_p = 0.25\overline{\eta^2}, \quad E_k = 0.5\overline{\overline{\left(\varphi_x^2 + \varphi_y^2 + \varphi_z^2\right)}}, \tag{28}$$

569 where single bar denotes averaging over the ξ and ϑ coordinates, while double bar denotes

570 averaging over entire volume. The derivatives in (25) are calculated according to transformation

571 (1). An equation of integral energy $E = E_p + E_k$ evolution can be represented in the following

572 form:

573
$$\frac{dE}{dt} = \overline{\overline{I}} + \overline{\overline{D_b}} + \overline{\overline{D_t}} + \overline{\overline{N}}, \qquad (29)$$

574 where $\overline{\overline{I}}$ is the integral input of energy from wind (Eqs. (14) – (18); $\overline{\overline{D_b}}$ is a rate of energy

575 dissipation due to the wave breaking (Eqs. (24) – (27)); $\overline{\overline{D_t}}$ is a rate of energy dissipation due to

576 filtration of high-wave number modes ('tail dissipation', Eqs. (19) – (23)); $\overline{\overline{N}}$ is an integral effect

577 of the nonlinear interactions described by the right-hand side of the equations when surface

578 pressure p is equal to zero. The differential form for calculation of the energy transformation can

579 be, in principle, derived from Eqs. (4) – (6), but here a more convenient and simple method was

580 applied. Different rates of integral energy transformations can be calculated with help of

581 fictitious time steps (i.e., apart from the basic calculations). For example, the value of $\overline{\overline{I}}$ is

582 calculated by the following relation:

583

584
$$\overline{\overline{I}} = \frac{1}{\Delta t}\left(\overline{\overline{E^{t+\Delta t}}} - \overline{\overline{E^{t}}}\right), \qquad (30)$$

585

586 where $\overline{\overline{E^{t+\Delta t}}}$ is the integral energy of wave field obtained after one time step with the right side of

587 equation (6) containing only the surface pressure calculated with Eqs. (14) – (18). For

588 calculation of the dissipation rate due to filtration, the right-hand side of the equations contains

589 just the terms introduced in Eqs. (19) - (23), while for calculation of the effects of breaking, only

590 the terms introduced in (24) – (27) are in use.

591   An evolution of the characteristics calculated by formula (30) is shown in Fig. 3.
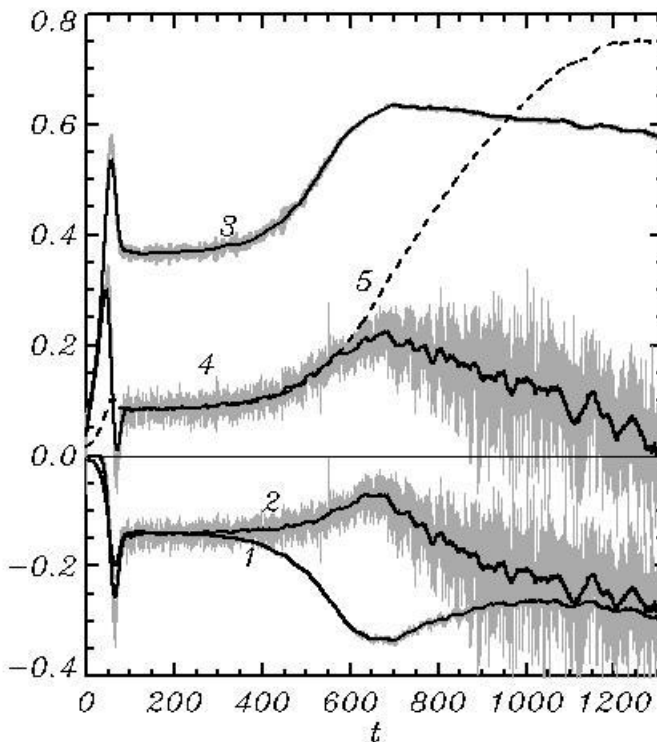
592

Figure 3. Evolution of integral characteristics of solution, rate of evolution of integral energy multiplied by 10^7) due to: 1 – tail dissipation D_t (Eqs. 19-23); 2 – breaking dissipation D_b (Eqs. 24-27); 3 – input of energy from wind I (Eqs. 14-18); 4 – balance of energy $I + D_t + D_b$. Curve 5 shows the evolution of wave energy $10^5 E$. Vertical bars of grey color show the instantaneous values; thick curve shows the smoothed behavior.

610

611

612

Sharp variations of all characteristics at $t < 50$ can be probably explained by adjustment of linear initial fields to nonlinearity. Up to the end of integration, the sum of all energy transition terms (tail dissipation $\overline{\overline{D_t}}$, breaking dissipation $\overline{\overline{D_b}}$ and energy input $\overline{\overline{I}}$) is approaching zero (curve 4), and the energy growth E (Curve 5) stops. Then the energy tends to decrease, but we are not sure about the nature of this effect. Such behavior can be explained by a fluctuating character of mutual adjustment of input and dissipation or simply by worsening of the approximation because of the downshifting process. Note that opposite to a more or less monotonic behavior of tail dissipation (Curve 1), the breaking dissipation is highly intermittent, which is consistent with common views on the nature of wave breaking.

The data on evolution of wave spectrum are shown in Fig. 4.
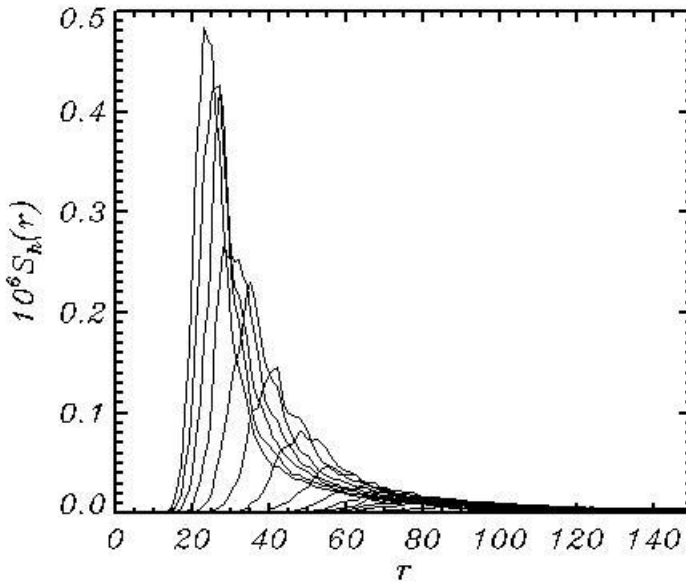
623

Figure 4. The wave spectra $S_h(r)$ integrated over angle ψ in the polar coordinates and averaged over consequent intervals of length about 100 units of nondimensional time t. The spectra are growing and shifting from right to left.

The 2-D wave spectrum $S(k,l)$ $\left(0 \le k \le M_x, -M_y \le l \le M_y\right)$ averaged over 13 time intervals of length equal to $\Delta t \approx 100$, was transferred to the polar coordinates $S_p(\psi, r)$ $\left(-\pi/2 \le \psi \le \pi/2, 0 \le r \le M_x\right)$ and then averaged over angle ψ to obtain 1-D spectrum $S_h(r)$:

$$S_h(r) = \sum S_p(\psi, r) r \Delta \psi . \tag{31}$$

An angle $\psi = 0$ coincides with the direction of wind U, $\Delta \psi = \pi/180$.
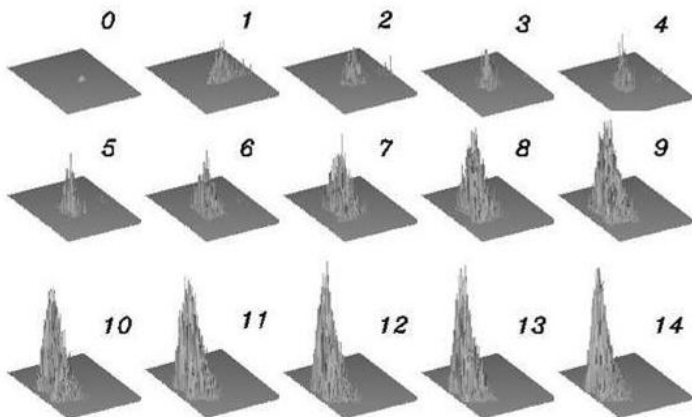
645

Figure 5. Sequence of 3-D images of $\lg_{10}(S(k,l))$ where each panel corresponds to single curve in Fig. 3. The left side refers to wave number $l\left(-M_y \le l \le M_y\right)$ and front side – to $k\left(0 \le k \le M\right)$. The numbers indicate

16

653   end of time interval expressed in hundreds of nondimensional time units.

654
655
656

657   As seen, each spectrum consists of separated peaks and holes[1]. This phenomenon was first
658   observed and discussed by Chalikov et al. (2014). The repeated calculations with different
659   resolution showed that such structure of 2-D spectrum is typical. It cannot be explained by fixed
660   combination of interacting modes, since in different runs (with the same initial conditions but
661   different set of phases for the modes) peaks are located in different locations in Fourier space.

662
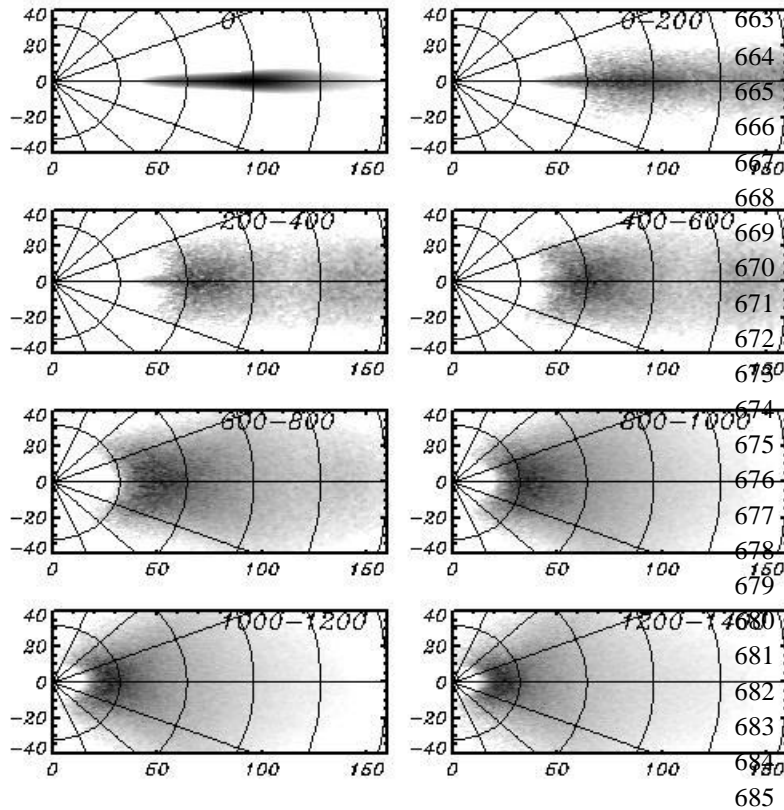
686   **Figure 6.** Sequence of 2-D images of $\lg_{10}\left(S(k,l)\right)$ averaged over consequent seven periods length $\Delta t = 200$.
687   Numbers indicate the period of averaging (first panel marked 0, refers to initial conditions). Horizontal and vertical
688   axes correspond to wave numbers *k* and *l* correspondingly

689

690   Another presentation is given in Fig 6 where the $\log_{10}\left(S(\psi,r)\right)$, averaged over the successive

691   seven period length $\Delta t = 200$, is given. The first panel with a mark 0 refers to initial conditions.

692   Disturbances within the range $(125 < k < 150)$ reflect initial adjustment of the input and

693   dissipation at high wave number slope of spectrum. The pictures characterize well the

694   downshifting and angle spreading of spectrum due to nonlinear interactions.

695   Evolution of the integrated over angles ψ wave spectrum $S_h(r)$ can be described with

696   the equation

697

---

[1]The wave spectrum looks rather like La Sagrada Familia (Gaudi) in Barcelona than the St. Mary
Axe ('Pickle') in London.

698
$$\frac{dS_h(r)}{dt} = I(r) + D_t(r) + D_b(r) + N(r),$$
(32)

699 where $I(r), D_t(r), D_b(r)$ and $N(r)$ are the spectra of the input energy, tail dissipation, breaking

700 dissipation and a rate of nonlinear interactions, all obtained by integration over angles ψ. All of

701 the spectra shown below were obtained by transformation of 2-D spectra into the polar

702 coordinate (ψ, r) and then integrated over angles ψ within the interval $(-\pi/2, \pi/2)$. The

703 spectra can be calculated using an algorithm similar to the algorithm (30) for integral

704 characteristics. For example, the spectrum of energy input $I(k,l)$ is calculated as follows:

705
$$I(k,l) = \left(S_c^{t+\Delta t}(k,l) - S_c^t(k,l) \right) / \Delta t,$$
(33)

706 where $S_c(k_x, k_y)$ is a spectrum of columnar energy calculated by relation

707
$$S_c(k,l) = \frac{1}{2}\left(h_{k,l}^2 + h_{-k,-l}^2 + \int_{-H}^{0} \left(u_{k,l}^2 + u_{-k,-l}^2 + v_{k,l}^2 + v_{-k,-l}^2 + w_{k,l}^2 + w_{-k,-l}^2 \right) d\zeta \right)$$
(34)

708 where grid values of velocity components u, v, w are calculated by relations:

709
$$u = \varphi_\xi + \varphi_\zeta \eta_\xi, \quad v = \varphi_\vartheta + \varphi_\zeta \eta_\vartheta, \quad w = \varphi_\zeta,$$
(35)

710 and $u_{k,l}, v_{k,l}$ and $w_{k,l}$ are their Fourier coefficients.

711 For calculation of $I(k,l)$ the fictitious time steps Δt are made only with a term

712 responsible for the energy input, i.e., surface pressure p. Spectrum $I(k,l)$ was averaged over the

713 periods $\Delta t \approx 100$, then transformed into a polar coordinate system and integrated in Fourier

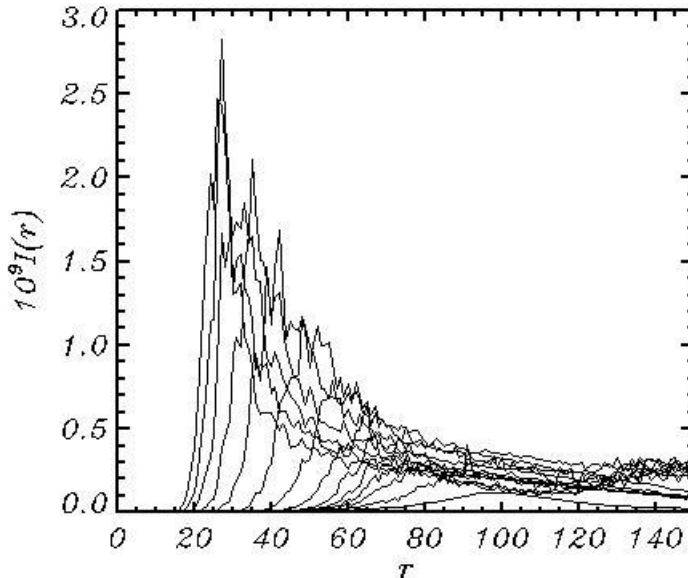714 space over angles ψ within the interval $(-\pi/2, \pi/2)$.

715

Figure 7. The spectrum of energy input $I(r)$ integrated over angle ψ in the polar coordinates and averaged over consequent intervals of length about 100 units of nondimensional time t.

732 The evolution of input spectra (Fig. 7) is, in general, similar to that of wave spectra shown in

733 Fig. 4. Note that a maximum of spectra is located at the maximum of wave spectra since the

734 input depends mainly on spectral density, while the dependence on frequency is less important.

735 Algorithm (32) − (35) was applied for calculation of the dissipation spectra due to

736 dumping of a high-wave number part of spectrum (tail dissipation) and for calculation of the

18

737 spectrum of breaking dissipation. In the first case, the fictitious time step was made taking into

738 account the terms described by Eqs (19) – (23), while in the second case the time step was made

739 using the terms described by Eqs (24) – (27).

740   The spectra of tail dissipation calculated similar to spectra $I(r)$ are shown in Fig. 8.

741 Dissipation occurs at the periphery of spectrum, outside the ellipse with semi-axes $d_m M_x$ and

742 $d_m M_y$ [2]. This is why such dissipation, averaged over angles, seems to affect a middle part of 1-D

743 spectrum. The tail dissipation effectively stabilizes the solution.

744   The breaking dissipation averaged over angles is presented in Fig. 8. As seen, the

745 breaking dissipation has a maximum at spectral peak. It does not mean that in the vicinity of

746 wave peak the probability of large curvilinearity is quite high. The high rate of breaking

747 dissipation can be explained by high wave energy in the vicinity of wave peak. The energy lost

748 through breaking, described by the diffusion mechanism, correlates with the energy of breaking

749 waves. Opposite to high wave number dissipation which regulates shape of spectral tail, the

750 breaking dissipation forms the main energy-containing part of spectrum.

751   The diffusion mechanism suggested in (24) - (27) modifies an elevation and surface

752 stream function in a close vicinity of breaking point. The amplitudes of side perturbation are

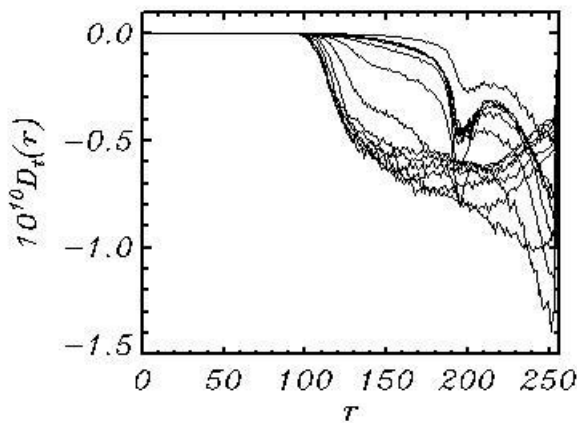753 small and decrease very quickly over the distance from a breaking point.

754

Figure 8. Tail dissipation spectra $D_t(r)$ integrated over angle ψ in the polar coordinates and averaged over consequent intervals of length about 100 units of nondimensional time t.
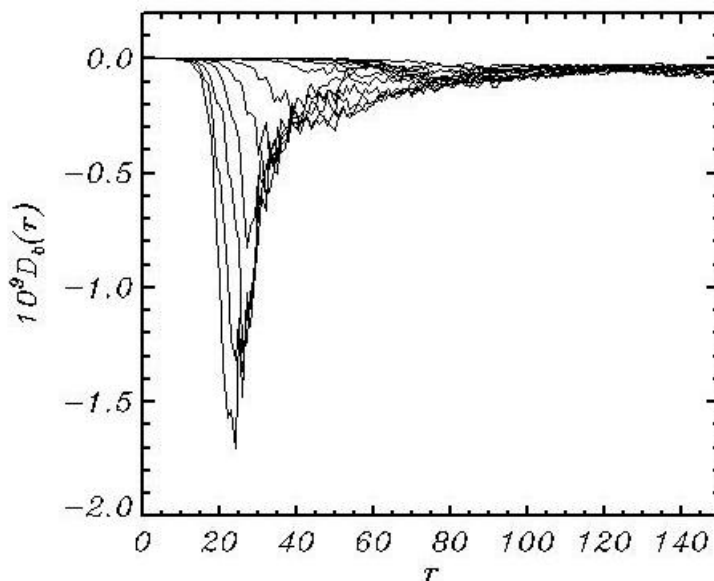
765

Figure 9. Breaking dissipation spectra $D_b(r)$ integrated over angle ψ in the polar coordinates and averaged over consequent intervals of length about 100 units of nondimensional time t.

---

[2]The 2-D Fourier spectral 'tail' looks like 'peacock' tail.

780

781   An example of profile of the energy input due to breaking $D_b(x)$ is given in Fig. 10. As

782   seen, energy input is fluctuating around the breaking point. A diffusion operator chosen for

783   breaking parameterization not only decreases total energy but also redistributes the energy

784   between Fourier modes in Fourier space.

785   In general, for the specific conditions considered in the paper, the breaking is an

786   occasional process taking place in a small part of domain. The kurtosis of input energy due to the

787   breaking $D_b(\xi, \vartheta)$, i.e., the value

788    $$Ku = \overline{\overline{D_b^4}} \left(\overline{\overline{D_b^2}} \right)^{-2} - 3 \qquad (36)$$

789   is of the order of 10^3, which corresponds to plain function with occasional separated peaks.

790
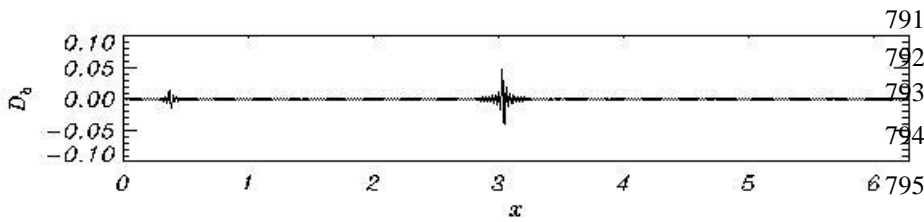
791

792   **Figure 10**. Example of
793   energy input due to
794   breaking $D_b(x)$.

795

796
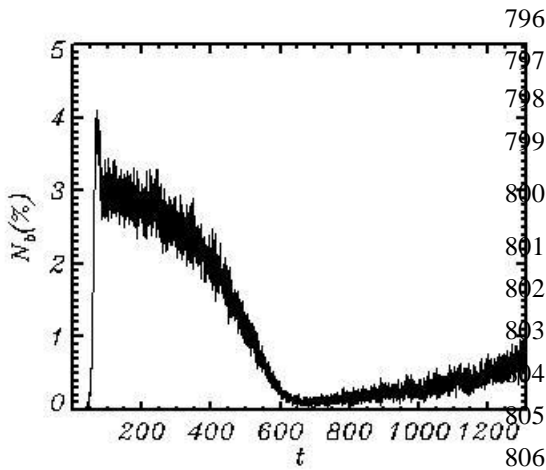
797
798   **Figure 11.** Evolution of number of wave breaking
799   events N_b expressed in percentage of the number
800   of grid points $N_x \times N_y$.

801
802
803
804
805
806
807

808   The number of breaking points in terms of percentage of the total number of points is given in

809   Fig. 11. As seen, the number of breaking events is going down to $t = 600$ and then is growing up

810   to the end of the calculations. The number of breaking events is not directly connected with

811   intensity of breaking, which is seen when comparing Fig. 11 and curve 2 in Fig.3.

812   An integral term describing nonlinear interaction $\overline{\overline{N}}$ in Eq. (29) is small (compared with local

813   values of $N_{k,l}$), but the magnitude of spectrum $N(r)$ is comparable with input $I(r)$ and

814   dissipation $D_t(r)$ and $D_b(r)$ terms. The presentation of term $N(r)$ in a form shown in Figs. (6)

815   – (8) is not clear. This is why the spectra $10^8 N(r)$ averaged over interval $\Delta t = 100$ are plotted

816   separately in Fig. 11 for the last eight intervals (thick curves) together with the wave spectrum

817    $10^6 S_h(r)$. In general, the shapes of spectrum $N(r)$ agree with the conclusions of the quasi-

818   linear Hasselmann (1962) theory (Hasselmann et al., 1985). At low wave number slope of

819   spectrum the nonlinear influx of energy is positive while at the opposite slope it is negative. This

820 process produces shifting of spectrum to the lower wave number (downshifting). Opposite to the
821 Hasselmann's theory, these results are obtained by solution of full three-dimensional equations.
822 It would be interesting to compare our results with the calculations of Hasselmann's integral
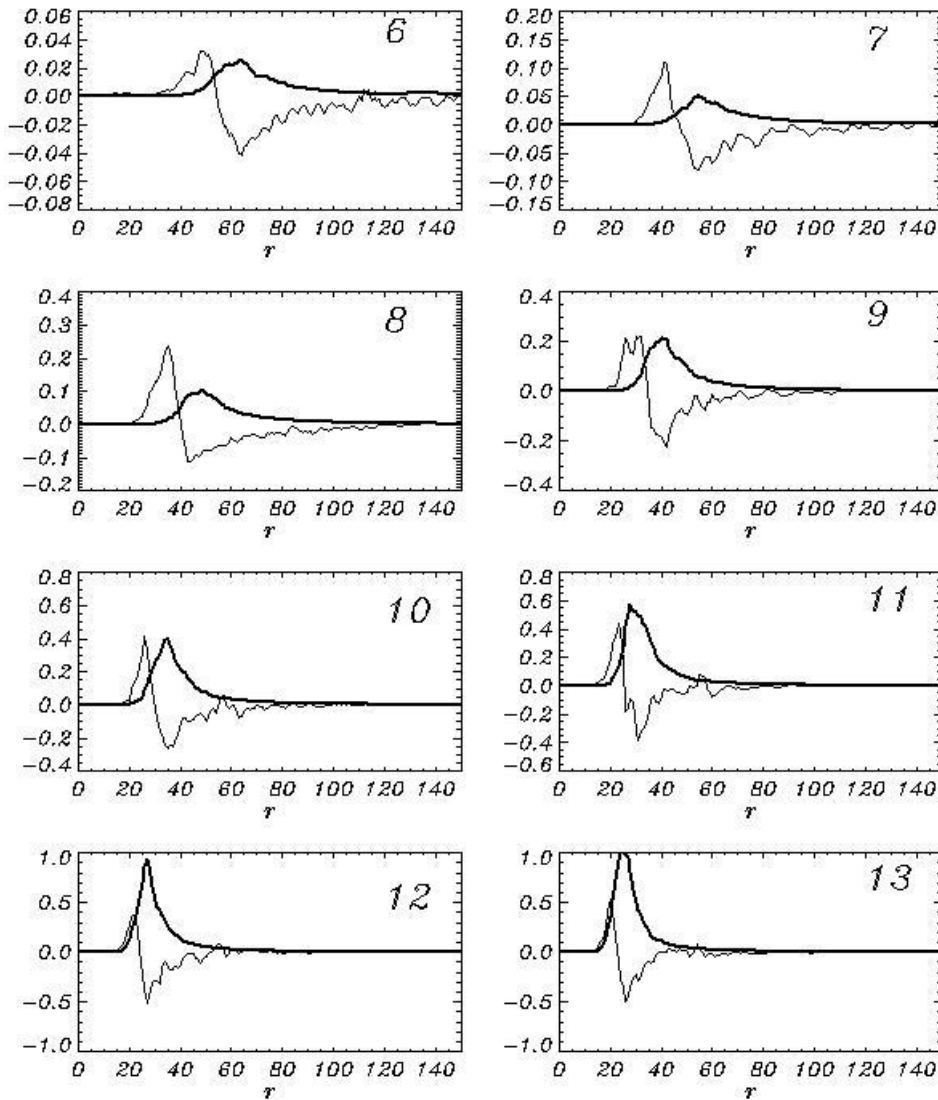823

Figure 12. Sequence of wave spectra $S_h(r)$ (thick curves) and nonlinear input term $N(r)$ (thin curves) averaged over consequent eight periods of length $\Delta t = 100$ starting from 6th period.

851 Unfortunately, neither of the existing programs of such type permits doing calculations with such
852 a high resolution that was used in the current model. Note that nonlinear interactions also
853 produce widening of spectrum.
854   Obviously, the nonlinearity is quite an important property of surface waves. The
855 contribution of nonlinearity can be estimated, for example, by comparison of the kinetic energy
856 of linear component $E_l = 0.5\overline{\left(\overline{\varphi_x^2} + \overline{\varphi_y^2} + \overline{\varphi_z^2}\right)}$ and the total kinetic energy E_k (Fig. 13). A ratio
857 E_l / E_k as a function of time remains very close to 1, which proves that the nonlinear part of
858 energy makes up just a small percentage of the total energy. It does not mean that the role of
859 nonlinearity is small; its influence can manifest itself over large time scales.
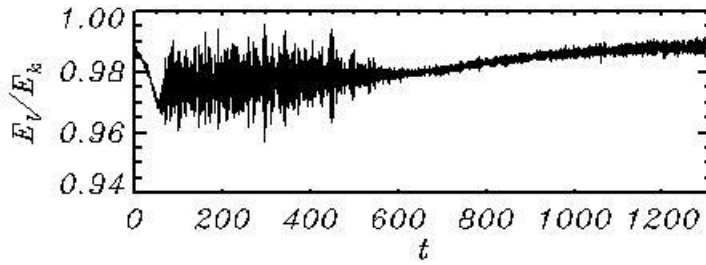860

861

862

Figure 13. Time evolution of ratio E_l / E_k .

868   The time evolution of integral spectral characteristics is presented in Fig. 14.
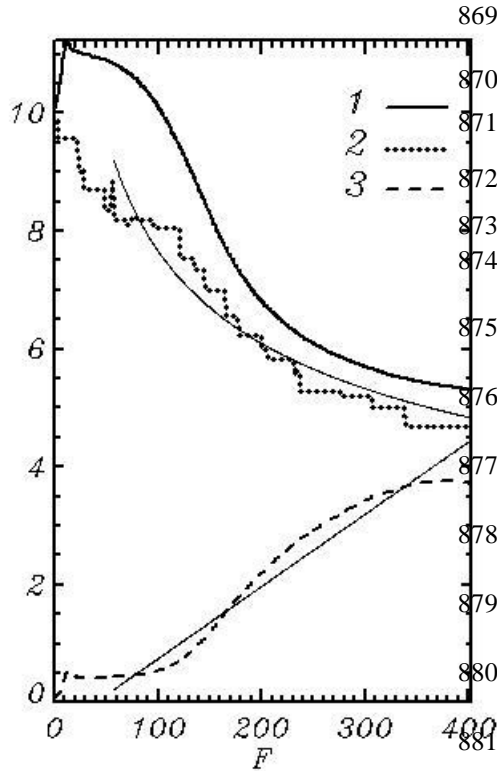
869

Figure 14. Time evolution of: weighted frequency ω_w (1) (Eq. 34); spectral peak frequency $\omega_p = k_p^{1/2}$ (2); full energy E (3) (Eq. 28). Thin curves are empirical a distance passed by the spectral peak.

882

883   Curve 1 corresponds to the weighted frequency ω_w

884        $$\omega_w = \left(\frac{\int kSdkdl}{\int Sdkdl} \right)^{1/2} ,$$ (37)

885   where integrals are taken over the entire Fourier-domain. The value ω_w is not sensitive to the

886   details of spectrum, hence, it well characterizes the position of spectrum and its shifting. Curve2

887   describes evolution of the spectral maximum. The step shape of curve corresponds to the

888   fundamental property of downshifting. Opposite to the common views, development of spectrum

889   occurs not monotonically, but by appearance of a new maximum at lower wave number as well

890   as by attenuation of the previous maximum. . Interesting that the same phenomenon is also

891   observed in spectral model (Rogers et al., 2012). Curve 3 describes the change of total energy

892    $E = E_p + E_k$. As seen all three curves have a tendency for slowing down of evolution rate. Then

893   the energy tends to decrease, but we are not sure about the nature of this effect. Such behavior

894   can be explained by a fluctuating character of mutual adjustment of input and dissipation or

895 simply by worsening of the approximation because of the downshifting process. The numerical
896 experiment reproduces the case when development of wave field occurs under the action of
897 permanent and uniform wind. This case corresponds to JONSWAP experiment. Despite large
898 scatter, the data allow us to construct empirical approximations of wave spectrum, as well as to
899 investigate the evolution of spectrum as a function of fetch F. In particular, it is suggested that
900 the frequency of spectral peak changes as $F^{-1/3}$, while full energy grows linearly with F. Neither
901 of the dependences can be exact, since they do not take into account the approaching to a
902 stationary regime. Besides, the dependence of frequency on fetch is singular at $F = 0$.

903 The value of fetch in periodic problem can be calculated by integration of peak phase
904 velocity $c_p = |k|^{-1/2}$ over time.

905
$$F = \int_{t_0}^{t} c_p dt \tag{38}$$

906 The JONSWAP dependencies for the frequency of spectral peak ω_p and full energy E are
907 shown in Fig 14 by thin curves. Dependence $\omega_p \sim F^{1/3}$ is qualitatively valid. Dependence of the
908 total energy on fetch does not look like a linear one, but it is worth to note that JONSWAP
909 dependence is evidently inapplicable to a very small and large fetch.

910
911 **5. Discussion**
912
913 A model based on the full three-dimensional equations of potential motion with free
914 surface was used for simulation of development of wave fields. The model is written in the
915 surface-following nonstationary non-orthogonal coordinate system. The details of numerical
916 scheme and the results of validation of the model were described in (Chalikov et al., 2014). The
917 main difference between the given model and HOS model (Ducroset et al., 2017) is that our
918 model is based on direct solution of 3-D equations for velocity potential. This approach is similar
919 to that developed at Technical University of Denmark (TUD, see Engsig-Karup et al., 2009).
920 Actually, the models developed at TUD are directed to solution of a variety of problems
921 including such problems as modeling of wave interaction with submerged objects and simulation
922 of wave regime in the basins with real shape and topography.
923 In the current paper a three-dimensional model was used for simulation of development
924 of wave field under the action of wind and dissipation. The input energy is described by single
925 term, i.e., surface pressure p in Eq. (4). It is traditionally assumed that the complex pressure
926 amplitude in Fourier space is linearly connected with the complex elevation amplitude with a
927 complex coefficient called β – function. Such simple formulations can be imperfect. Firstly, it is
928 assumed that wave field is represented by superposition of linear modes with slowly changing
929 amplitudes and phase velocity obeying the linear dispersive relation. This assumption is valid
930 only for a low-frequency part of spectrum. In reality, the amplitudes of medium and high-
931 frequency modes undergo fluctuations created by reversible interactions. A solid dispersion
932 relation does not connect their phase velocities with wave number. Besides, it is also quite
933 possible that the suggestion of linearity of the connection between pressure and elevation
934 amplitudes is not precise, i.e., β – function can depend on amplitudes of modes.

935   We are not familiar with any observational data that can be used for formulation of
936 statistically provided scheme for calculation of the input energy to waves. The only method that
937 can give more or less reliable results is mathematical modeling of the statistical structure of
938 turbulent boundary layer above a curvilinear moving surface, of which characteristics satisfy
939 kinematic conditions. The method described above is based on several millions values of
940 pressure referred strictly to surface. As a whole, the problem of boundary layer seems even more
941 complicated than the wave problem itself. Some early attempts to solve this problem were made
942 on the basis of the finite difference two-dimensional model of boundary layer written in the
943 simple surface following coordinate (see review Chalikov, 1986). Waves were assigned as a
944 superposition of linear modes with random phases corresponding to the empirical wave
945 spectrum. This approach was not quite accurate since it did not take into consideration the
946 nonlinear properties of surface (for example, the sharpness of real waves and the absence of
947 dispersive relation for waves of medium and high frequencies. The next step was formulation of
948 coupled models for boundary layer and potential waves, both written in the conformal
949 coordinates (Chalikov and Rainchik, 2014). The calculations showed that pressure field consists
950 mostly of random fluctuations not directly connected with waves. A small part of these
951 fluctuations is in phase with surface disturbances. The calculated values of β in Eq. (13) have
952 large dispersion. However, since the volume of data was very large, the shape of β-function was
953 found with high-level accuracy. Probably, approximation of β used in the current work can be
954 considered as most adequate. We are planning additional investigations based on coupled wind-
955 wave models. The next step in investigations of Wave boundary Layer (WBL)should use a
956 three-dimensional LES approach. Note that even availability of large volume of data on the
957 structure of WBL does not make the problem of parameterization of wind input in spectral wave
958 models easily solvable, since the pressure is characterized by a broad continuous spectrum
959 created by nonlinearity.
960   The wave breaking is obviously even more complicated than the input energy.
961 Nevertheless, this problem can be simplified, if common ideas used in the numerical fluid
962 mechanics are accepted. For example, in LES modeling the more or less artificial viscosity is
963 introduced to prevent too large local velocity gradients. It is a fact that the numerical instability
964 terminating computations precedes wave breaking. Hence, the scheme should prevent breaking
965 approach to preserve stability of the numerical scheme. Hence, a wave model should contain the
966 algorithms preventing appearance of too large slopes. The criterion of breaking is introduced not
967 for recognizing of the breaking itself, but for the choice of places where it might happen (or,
968 unfortunately, might not happen). Finally, the algorithm should produce local smoothing of
969 elevation (and surface potential). The algorithm should be highly selective so that 'breaking'
970 would occur within narrow intervals and not affect the entire area. The exact criteria of breaking
971 events (most evident of them is the breaking itself) cannot be used for parameterization of
972 breaking since in coordinate system (1) the numerical instability occurs long before breaking. In
973 our opinion, the most sensitive parameter indicating potential instability is the curvilinearity
974 (second derivative) of elevation.
975   In the current work, the breaking is parameterized by diffusion algorithm with the
976 nonlinear coefficient diffusion providing high selectivity of smoothing. We admit that such
977 approach can be realized in many different forms. The same situation is observed in a problem of
978 turbulence modeling for parameterization of subgrid scales. Note, that breaking dissipation in
979 phase resolving models is included in more realistic manner, that in spectral models. For

example, the breaking is simulated in physical space, what allows to reduce the height and energy of nonlinear waves, composed of several modes, In spectral models dissipation is distribute more or less arbitrarily over entire spectrum. Spectral models sometimes include the additional dissipation of short waves due to their modulation by long waves (Young and Babanin, 2006; Babanin et al., 2010). In phase resolving models this process have been included explicitly.

We can finally conclude that the physics included in the wave model is still based on a shaky ground. Nevertheless, the result of the calculations looks quite realistic, which convinces us that the approach deserves further development.

The numerical models of waves similar to that considered in the paper have a lot of important applications. Firstly, they are a perfect tool for development of physical parameterizations schemes in spectral wave models. Secondly, the direct model can be used in future for numerical simulation of wave processes in the basins of small and medium size. These investigations can be based on HOS model (Ducrozet et al., 2016) or the model used in the current paper. However, the most universal approach seems to be developed at the Technical University of Denmark (see Engsig-Karup, 2009). Any model used for a long-term simulation of wave field evolution should include the algorithms describing transformation of energy, similar to those considered in the current paper.

References

Alberello, A., A. Chabchoub, J. P. Monty, F. Nelli, J. H. Lee, J. Elsnab, and A. Toffoli. An experimental comparison of velocities underneath focused breaking waves. Ocean Engineering, 155, 201-210 2018

Alves, J. H. G. M., and Banner, M. L. Performance of a Saturation-Based Dissipation-Rate Source Term in Modeling the Fetch-Limited Evolution of Wind Waves. J. of Phys. Oceanography, 33, 1274-1298, 2003

Al'Zanaidi, M. A. and Hui, H. W. Turbulent airflow over water waves-a numerical study. J. Fluid Mech., 148, 225-246 1984

Babanin, A. V., Tsagareli, K. N., Young, I. R. and Walker D. J. Numerical Investigation of Spectral Evolution of Wind Waves. Part II: Dissipation Term and Evolution Tests. J. of Phys. Oceanography, 40 (4), 667-683, 2010

Babanin, A.V., Breaking and Dissipation of Ocean Surface Waves. Cambridge University Press, 480pp. 2011

Beale, J. T. A convergent boundary integral method for three-dimensional water waves, *Math. Comput.* 70 pp 977–1029, 2001

Bonnefoy, F., Ducrozet, G., Le Touzé, D. and Ferrant, P. Time-domain simulation of nonlinear water waves using spectral methods. In *Advances in Numerical Simulation of Nonlinear Water Waves*, Vol. 11*, Advances in Coastal and Ocean Engineering*. World Scientific, 129–164; doi:10.1142/9789812836502_0004. Google book, 2010

Causon, D. M., Mingham, C. G., and Qian, L. Developments In Multi-Fluid Finite Volume Free Surface Capturing Methods. *Advances in Numerical Simulation of Nonlinear Water Waves*: pp. 397-427, 2010

Chalikov, D.V. Numerical simulation of wind-wave interaction. J. Fluid. Mech. 87, 561-582, 1978

Chalikov, D.V.: Numerical simulation of the boundary layer above waves. Bound. Layer Met., 34. 63-98, 1986

Chalikov, D.: The Parameterization of the Wave Boundary Layer. J. Phys. Oceanogr., 25, 1335-1349, 1995

Chalikov, D.: Statistical properties of nonlinear one-dimensional wave fields. Nonlinear processes in geophysics. 12, 1-19, 2005

Chalikov, D.: Freak waves: their occurrence and probability. Phys of Fluid, 21, 076602, 2009

Chalikov, D.: Numerical modeling of sea waves, Springer, DOI 10.1007/978-3-319-32916-1, 330 pp. 2016

Chalikov, D. and Makin, V.: Models of the wave boundary layer. Bound. Layer Met., 56, 83-99, 1991

Chalikov, D. and Belevich, M.: One-dimensional theory of the wave boundary layer. Bound. Layer Met., 63, 65-96, 1992

Chalikov, D. and Sheinin, D.: Direct Modeling of One-dimensional Nonlinear Potential Waves. Nonlinear Ocean Waves, ed. W. Perrie, Advances in Fluid Mechanics, 17, 207- 258, 1998

Chalikov, D., Babanin, A. V. and Sanina, E.: Numerical Modeling of Three-Dimensional Fully Nonlinear Potential Periodic Waves. Ocean dynamics. 64, 10, 1469-1486, 2014

Chalikov, D. and Rainchik, S.: Coupled Numerical Modelling of Wind and Waves and the Theory of the Wave Boundary Layer. Boundary-Layer Meteorol. 138:1–41. DOI 10.1007/s10546-010-9543-7, 2010

Chalikov, D. and Babanin, A. V.,: Simulation of Wave Breaking in One-Dimensional Spectral Environment. Journal Phys. Ocean., Vol. 42, No. 11, 1745-1761, 2012

Chalikov D. and Babanin A.V.: Simulation of one-dimensional evolution of wind waves in a deep water. Physics of fluid, 26 (9), 096607, 2014

Chalikov D. and Babanin A.V.: Nonlinear sharpening during superposition of surface waves. Ocean Dynamics. 66(8), 931-937, 2016a

Chalikov D. and Babanin A.V.: Comparison of linear and nonlinear extreme wave statistics. Acta Oceanologica Cinica. 35,5,99-105, DOI:10,1007/313131-016-0862-5, 2016b

Clamond, D. and Grue J. (2001). A fast method for fully nonlinear water wave dynamics, *J. Fluid Mech*. 447, 337-355, 2005

Clamond, D., Fructus, D., Grue, J. and Krisitiansen O. An efficient method for three-dimensional surface wave simulations. Part II: Generation and absorption. *J. Comp. Physics*, 205, pp 686-705, 2005

Clamond, D., Francius, M,. Grue, J., Kharif, C. Long time interaction of envelope solitons and freak wave formations. *European Journal of Mechanics* B/Fluids 25, pp 536–553, 2006

Dalrymple, R. A., Gómez-Gesteira, M., Rogers, B. D., Panizzo, A., Zou, S., Crespo, A. J,. Cuomo, G. and Narayanaswamy M. (2010). Smoothed Particle Hydrodynamics For Water Waves. *Advances in Numerical Simulation of Nonlinear Water Waves:* pp. 465-495, 2010

Dommermuth, D., Yue, *D*. A high-order spectral method for the study of nonlinear gravity Waves. *J. Fluid Mech*., 184, pp 267–288. 1987

Donelan, M.A., Babanin A.V. Young I.R., Banner, M.L., and McCormick, C.: Wave follower field measurements of the wind input spectral function. Part I. Measurements and calibrations. J. Atmos. Oceanic tech. 22, 799-813, 2005

Donelan, M.A., Babanin A.V. Young I.R. and Banner, M.L.: Wave follower field measurements of the wind input spectral function. Part II. Parameterization of the wind input. J. Phys. Oceanogr. 36, 1672-1688, 2006

Dysthe, K. B.: Note on a modification to the nonlinear Schrödinger equation for application to deep water waves. *Proc. R. Soc. Lond.* A **369**, 105–114, 1979

Ducrozet, G., Bonnefoy, F., Le Touzé, D., and Ferrant, P. 3-D HOS simulations of extreme waves in open seas, *Nat. Hazards Earth Syst. Sci.*, 7, pp 109-122; doi:10.5194/nhess-7-109-2007, 2007

Ducrozet, G., Bingham H. B., Engsig-Karup A. P., Bonnefoy F. and Ferrant P. A comparative study of two fast nonlinear free-surface water wave models. *Int. J. Numer. Meth. Fluids,* **69**, pp 1818–1834, 2012

Ducrozet G., Bonnefoy F., Le Touzé D. and Ferrant P.: HOS-ocean: Open-source solver for nonlinear waves in open ocean based on High-Order Spectral method. Comp. Phys. Comm., doi:10.1016/j.cpc.2016.02.017, 2016

Engsig-Karup, A.P., Harry B., Bingham H.B. and Lindberg O.: An efficient flexible-order model for 3D nonlinear water waves. J. Comput. Physics 228(6), 2100-2118, 2009

Engsig-Karup, A., Madsen M. and Glimberg S. A massively parallel GPU-accelerated mode for analysis of fully nonlinear free surface waves. *International Journal for Numerical Methods in Fluids*. 10.1002/fld. 2675, 2012

Fochesato, C. Dias, F. and Grilli, S. Wave energy focusing in a three-dimensional numerical wave tank. *Proc. R. Soc*. A 462, pp 2715–2735, 2006

Fructus, D., Clamond, D., Grue J, and Kristiansen, Ǿ. An efficient model for three- dimensional surface wave simulations. Part I: Free space problems, *J. Comp. Phys*. 205, 665–68, 2005

Gent, P. R. & Taylor, P. A. A numerical model of the air flow above water waves. *J. Fluid Mech.* **77**, 105–128, 1976

Gou, Y., Teng, B., Yoshida, S. An Extremely Efficient Boundary Element Method for Wave Interaction with Long Cylindrical Structures Based on Free-Surface Green's function. *Computation*, *4*, 36. 2016

Craig, W., and Sulem C. Numerical simulation of gravity waves, *J. Comput. Phys*. 108, pp 73–83, 1993

Greaves, D. Application Of The Finite Volume Method To The Simulation Of Nonlinear Water Waves. *Advances in Numerical Simulation of Nonlinear Water Waves*: pp. 357-396, 2010

Grilli, S., Guyenne, P., Dias, F. A fully nonlinear model for three-dimensional overturning waves over arbitrary bottom. Int. *J. Num. Methods Fluids,*, 3**5**, pp 829–867, 2001

Grue, J., and Fructus, D. Model For Fully Nonlinear Ocean Wave Simulations Derived Using Fourier Inversion Of Integral Equations In 3D. *Advances in Numerical Simulation of Nonlinear Water Waves:* 1-42, 2010

Guyenne, P., Grilli S. T. Numerical study of three-dimensional overturning waves in shallow water, *J. Fluid Mech*. 547, 361–388, 2006

Hasselmann, K.: On the non-linear energy transfer in a gravity wave spectrum, Part 1, . J. Fluid Mech., 12, 481–500, 1962

Hasselmann, S., K. Hasselmann, J. H. Allender, and T. P. Barnett, 1985: Computations and Parameterizations of the Nonlinear Energy Transfer in a Gravity-Wave Specturm. Part II: Parameterizations of the Nonlinear Energy Transfer for Application in Wave Models. J. of Phys. Oceanography, 15 (11), 1378-1392, 1985

Hasselmann, K, Barnett R. P., and Bouws, et al.: Measurements of wind-wave growth and swell decay during the Joint Sea Wave Project (JONSWAP). Tsch. Hydrogh. Z. Suppl. 1973, A8(12), 1-95, 1973

Hasselmann, D., and J. Bösenberg,: Field measurements of wave-induced pressure over wind-sea and swell. J. Fluid Mech., **230,** 391–428, 1991

Hsiao, S. V., and O. H. Shemdin,: Measurements of wind velocity and pressure with a wave follower during MARSEN. J. Geophys. Res., 88**,** 9841–9849, 1983

Iafrati, A.: Numerical Study of the Effects of the Breaking Intensity on Wave Breaking Flows. J Fluid Mech,, 622, 371-411, 2009

Issa, R, Violeau, D, Lee E.-S. and Flament H. Modelling nonlinear water waves with RANS and LES SPH models. *Advances in Numerical Simulation of Nonlinear Water Waves*: 497-537, 2010

Kim, K. S., Kim M. H., and Park J. C. Development of MPS (Moving Particle Simulation) method for Multi-liquid-layer Sloshing," *Journal of Mathematical Problems in Engineering*, Vol. 2014, doi:10.1155/2014/350165, 2014

Liu, Y., Gou, Y., Bin Teng. B. and Shigeo Yoshida S. An Extremely Efficient Boundary Element Method for Wave Interaction with Long Cylindrical Structures Based on Free-Surface Green's Function. *Computation*, *4*(3), 36; doi:10.3390/computation4030036, 2016

Lubin, P. and Caltagirone J.-P. Large eddy simulation of the hydrodynamics generated by breaking waves. *Advances in Numerical Simulation of Nonlinear Water Waves*: pp. 575-604, 2010

Ma, Q. W., and Yan, S. Qale-FEM method and its application to the simulation of free responses of floating bodies and overturning waves. *Advances in Numerical Simulation of Nonlinear Water Waves:* pp. 165-202, 2010

Miles, J.W. 1957: On the generation of surface waves by shear flows. J. Fluid Mech,3, 02, doi: 10.1017/S0022112057000567, 1957

Rogers, W.E., Babanin, A.V. and Wang, D.W.: Observation-consistent input and whitecapping-dissipation in a model for wind-generated surface waves: Description and simple calculations. J. Atmos. Oceanic Tech., 29(9), 1329-1346, 2012

Snyder, R. L., Dobson, F.W., Elliott, J.A., and Long, R.B.: Array measurements of atmospheric pressure fluctuations above surface gravity waves. J. Fluid Mech., 102**,** 1–59, 1981

Tanaka, M. Verification of Hasselmann's energy transfer among surface gravity waves by direct numerical simulations of primitive equations. *Journal of Fluid Mechanics*; 444, pp 199–221, 2001

Ting C.-H, Babanin, A.V., Chalikov, D. and Tai-Wen Hsu,: Dependence of drag coefficient on the directional spreading of ocean waves, J. Geophys. Res., 117, C00J14, doi:10.1029/2012JC007920, 2012

Toffoli, A., Onorato M., Bitner-Gregersen E., Monbaliu J. Development of a bimodal structure in ocean wave spectra. *Journal of Geophysical Research*; 115:C03006. DOI: 10.1029/2009JC005495, 2010

Tolman, H. and Chalikov, D. On the source terms in a third-generation wind wave model. Journ. Phys. Oceanogr. 1996, 26, 2497-2518, 1996

Tolman, H.,L and the WAVEWATCH III °R Development Group: User manual and system documentation of WAVEWATCH III °R version 4.18 Environmental Modeling Center Marine Modeling and Analysis Branch, Contribution No. 316, 2014

Touboul, J. and Kharif, C. Two-Dimensional Direct Numerical Simulations Of The Dynamics Of Rogue Waves Under Wind Action. *Advances in Numerical Simulation of Nonlinear Water Waves*: pp. 43-74, 2010

West, B., Brueckner, K., Janda, R., Milder, M., Milton, R. A new numerical method for surface hydrodynamics, *J. Geophys. Res.*, 92, pp 11 803–11 824, 1987

Young, I. R., and Babanin, A.V. Spectral Distribution of Energy Dissipation of Wind-Generated Waves due to Dominant Wave Breaking. Journal of Physical Oceanography, 36 (3), 376-394, 2006

Young, D-L, Wu, N-J, and Tsay, T-K. Method Of Fundamental Solutions For Fully Nonlinear Water Waves. *Advances in Numerical Simulation of Nonlinear Water Waves:* pp. 325-355, 2010

Xue M., Xu, H., Liu, Y., Yue, D. K. P. Computations of fully nonlinear three-dimensional wave and wave–body interactions. I. Dynamics of steep three-dimensional waves, *J. Fluid Mech.* 438, pp 11–39, 2001

Zakharov, V. E. Stability of periodic waves of finite amplitude on the surface of deep fluid. *J. Appl. Mech. Tech. Phys. JETF* (English translation). **2,** pp 190-194, 1968

Zhao, X. & Liu, B.-J & Liang, S.-X & Sun, Z.-C. Constrained Interpolation Profile (CIP) method and its application. Chuan Bo Li Xue/Journal of Ship Mechanics. 20. pp. 393-402. 10.3969/j.issn.1007-7294.2016.04.002, 2016

Figure captions

Figure 1. Real (dashed curve) and imaginary (solid curve) parts of β-function.

Figure 2. Probability of curvilinearity $\eta_{\xi\xi}$. Thick curve calculated with full 3-D model; thin curve is a probability calculated over ensemble of linear modes with the same spectrum.

Figure 3. Evolution of integral characteristics of solution, rate of evolution of integral energy multiplied by 10^7) due to: 1 – tail dissipation D_t (Eqs. 19-23); 2 – breaking dissipation D_b (Eqs. 24-27); 3 – input of energy from wind I (Eqs. 14-18); 4 – balance of energy $I + D_t + D_b$. Curve 5 shows the evolution of wave energy $10^5 E$. Vertical bars of grey color show the instantaneous values; thick curve shows the smoothed behavior.

Figure 4. The wave spectra $S_h(r)$ integrated over angle ψ in the polar coordinates and averaged over consequent intervals of length about 100 units of nondimensional time t. The spectra are growing and shifting from right to left.

Figure 5. Sequence of 3-D images of $\lg_{10}(S(k,l))$ where each panel corresponds to single curve in Fig. 3. The left side refers to wave number $l(-M_y \le l \le M_y)$ and front side – to $k(0 \le k \le M)$. The numbers indicate end of time interval expressed in hundreds of nondimensional time units.

Figure 6. Sequence of 2-D images of $\lg_{10}(S(k,l))$ averaged over consequent seven periods length $\Delta t = 200$. Numbers indicate the period of averaging (first panel marked 0, refers to initial conditions). Horizontal and vertical axes correspond to wave numbers k and l correspondingly

Figure 7. The spectrum of energy input $I(r)$ integrated over angle ψ in the polar coordinates and averaged over consequent intervals of length about 100 units of nondimensional time t.

1200   **Figure 8.** Tail dissipation spectra $D_t(r)$ integrated over angle ψ in the polar coordinates and

1201   averaged over consequent intervals of length about 100 units of nondimensional time t.

1202   **Figure 9.** Breaking dissipation spectra $D_b(r)$ integrated over angle ψ in the polar coordinates

1203   and averaged over consequent intervals of length about 100 units of nondimensional time t.

1204   **Figure 10**. Example of energy input due to breaking $D_b(x)$.

1205   **Figure 11.** Evolution of number of wave breaking events N_b expressed in percentage of the

1206   number of grid points $N_x \times N_y$.

1207   **Figure 12.** Sequence of wave spectra $S_h(r)$ (thick curves) and nonlinear input term $N(r)$ (thin

1208   curves) averaged over consequent eight periods of length $\Delta t = 100$ starting from 6th period.

1209   **Figure 13.** Time evolution of ratio E_l / E_k

1210   **Figure 14.** Time evolution of: weighted frequency ω_w (1) (Eq. 34); spectral peak frequency

1211 $\omega_p = k_p^{1/2}$ (2); full energy E (3) (Eq. 28). Thin curves are empirical a distance passed by the

1212   spectral peak.